

Amorphous and crystalline ice on the Galilean satellites: A balance between thermal and radiolytic processes

Gary B. Hansen

Pacific Northwest Division, Planetary Science Institute, Department of Earth and Space Science, University of Washington, Seattle, Washington, USA

Thomas B. McCord

Pacific Northwest Division, Planetary Science Institute, Winthrop, Washington, USA

Hawaii Institute of Geophysics and Planetology, University of Hawaii at Manoa, Manoa, Hawaii, USA

Received 28 June 2003; revised 31 October 2003; accepted 26 November 2003; published 29 January 2004.

[1] The water ice on the three outermost Galilean satellites of Jupiter has a lattice structure that can vary from crystalline to amorphous. Amorphous ice is crystallized by heating, while crystalline ice is amorphized through disruption by particle radiation. We determine ice lattice order using infrared spectra from the Near Infrared Mapping Spectrometer on the Galileo Jupiter orbiter. The shape of the reflectance peak near $3.1\ \mu\text{m}$ is diagnostic of the lattice order in the top micrometers of the surface. A narrow, temperature-sensitive band near $1.65\ \mu\text{m}$, from $\sim 1\ \text{mm}$ depth, is missing for amorphous ice. Spectral averages of >100 pixels were used for Europa and Callisto, because of high radiation noise and small ice amounts, respectively. Model comparisons show that the surface ice is predominantly amorphous on Europa and predominantly crystalline on Callisto, while both types of ice are found on Ganymede. The distribution of Ganymede ice properties shows a broad global pattern of more amorphous ice in the high-latitude Jovian-facing hemisphere and in the low-latitude trailing hemisphere. The ice at $\sim 1\ \text{mm}$ depth on all three satellites is predominantly crystalline. The radiation flux increases by ~ 300 times between Callisto and Europa, while the thermal crystallization rate may vary over five orders of magnitude among the three satellites (being the fastest at Callisto). The occurrence of crystalline and amorphous ice suggests a balance between the disruption and crystallization, with Callisto dominated by thermal crystallization and Europa by radiative disruption, and with nearly equal rates between the two processes at Ganymede. **INDEX TERMS:** 6218 Planetology: Solar System Objects: Jovian satellites; 6020 Planetology: Comets and Small Bodies: Ice; 6025 Planetology: Comets and Small Bodies: Interactions with solar wind plasma and fields; 6045 Planetology: Comets and Small Bodies: Physics and chemistry of materials; 6061 Planetology: Comets and Small Bodies: Remote sensing; **KEYWORDS:** amorphous ice, crystalline ice, Europa, Ganymede, Callisto, radiation effects

Citation: Hansen, G. B., and T. B. McCord (2004), Amorphous and crystalline ice on the Galilean satellites: A balance between thermal and radiolytic processes, *J. Geophys. Res.*, *109*, E01012, doi:10.1029/2003JE002149.

1. Introduction

[2] Water ice is abundant on the three outermost Galilean Satellites of Jupiter, Europa, Ganymede, and Callisto [Sill and Clark, 1982]. It is identified by several distinctive, strong absorption bands found in the near-infrared spectra of these satellites [e.g., Kuiper, 1961; Moroz, 1965; Johnson and McCord, 1971; Pilcher et al., 1972; Clark and McCord, 1980; Clark et al., 1980; Clark, 1982]. The behavior of these bands in hemispherically resolved telescopic spectra has led to predictions of ice abundance and grain size on all

three satellites [Pollack et al., 1978; Clark and McCord, 1980; Clark et al., 1986; Roush et al., 1990; Calvin and Clark, 1991]. The ice bands in spatially resolved satellite spectra returned by the Near-Infrared Mapping Spectrometer (NIMS) [Carlson et al., 1996] on the Galileo Jupiter orbiter (1996–2000) have not been heretofore analyzed in detail. McCord et al. [1998, 1999a] present an overview of NIMS spectra of the icy satellites. The presence, shape, and position of all of these bands are functions of temperature, and of the lattice order (from crystalline to amorphous) in the ice. We use NIMS spectra ($0.7\text{--}5.3\ \mu\text{m}$) to study the lattice order of the surface ice on all three satellites. Although the band structure in the near-infrared changes throughout, the most striking effects of temperature and

lattice order are manifested in the behavior of a narrow band near 1.65 μm and in the spectral structure in the fundamental stretching band near 3.1 μm . We perform detailed analyses of NIMS spectra in these wavelength regions to determine the distribution of crystalline and amorphous surface ice on Europa, Ganymede, and Callisto. Preliminary results from this analysis have been presented previously [Hansen and McCord, 2000]. Although determining relative ice abundance and grain sizes are part of this analysis, a comprehensive study of these ice properties will be presented elsewhere.

[3] The most stable lattice structure (lowest energy or largest negative energy) for water ice at zero pressure is an hexagonal arrangement. Other arrangements occur at cold temperatures (<200 K) when the lattice does not have time to relax into the lowest energy state. They include a metastable cubic crystalline structure (in which the alternate planes of the hexagonal structure are shifted one position), and various disordered amorphous structures. The spectrum of hexagonal and cubic ice are indistinguishable from each other at wavelengths <70 μm [Bertie and Whalley, 1964, 1967], and the difference of internal energy between cubic and hexagonal ice is small [Handa et al., 1988]. The amorphous forms have highly variable spectra, depending on their age and temperature history. "Annealed" forms of amorphous ice (that have been warmed above 100 K) have well-determined, repeatable spectra [Hagen et al., 1981; Schmitt et al., 1998] that are distinct from the spectra of crystalline ice.

[4] The lattice order of ice is known to be dependent on its condensation temperature, condensation rate, and its temperature history [Jenniskens et al., 1998]. The temperature of the Galilean satellite surfaces is in a range (90–160 K) [Spencer et al., 1999] where any amorphous surface ice will crystallize over timescales ≤ 1 million years [Jenniskens et al., 1998; Kouchi et al., 1994]. Ice in the laboratory will crystallize almost instantly at 140–150 K, while the daytime temperature of the ice on the Jovian satellites is in the range 115–130 K. The ice temperatures are determined from thermal models of surfaces with segregated ice and non-ice patches [Spencer, 1987], in contrast to the mixed temperatures of ice and warmer soil that are typically measured by remote sensing at large spatial scales [e.g., Orton et al., 1996; Spencer et al., 1999]. The temperature of the segregated ice on Ganymede and Callisto has been measured with some precision from hemispheric telescopic spectra by Grundy et al. [1999] to be 123.8 ± 19 and 114.7 ± 18 K, respectively, using the temperature dependent properties of the near-infrared spectrum of the ice. These values are almost statistically equal, and many of the fits to Ganymede spectra were poor, perhaps because of the hydrated non-ice surface material [McCord et al., 2001]. Our guess is that the ice on Callisto is probably slightly warmer than on Ganymede, because Callisto's typical radiative environment includes more and warmer non-ice materials [cf. Moore et al., 1999]. So in general, the measurements imply that the segregated ice on Ganymede and Callisto assumes daytime temperatures of 115 ± 10 K. Kinetic models and studies of ice indicate that crystallization at 115 K will occur within 1 y to cubic ice, and a few $\times 10^8$ y to hexagonal ice [Jenniskens et al., 1998; Kouchi et al., 1994]. European ice may be somewhat colder

than ice on the other satellites because of its higher albedo environment, and would remain amorphous for a somewhat longer time (e.g., ~ 10 y to cubic ice at 100 K).

[5] New amorphous ice can be created from the condensation of vapor on the poles or night side (assuming that the growth rate is fast enough [Kouchi et al., 1994]), or from the flash freezing of cryovolcanic liquids. Another likely source of amorphous ice in the Jovian environment is the disruption of crystalline ice by corpuscular radiation, which is heavy and widespread among the Galilean satellites [Cooper et al., 2001, and references therein]. Radiation is known to cause disorder in crystalline ice, although the process appears to be much more effective at temperatures below 80–100 K in the laboratory [Strazzulla et al., 1992; Baratta et al., 1994]. The particle masses and energy distribution of the radiation seen in the Jovian system is far greater than achievable in most terrestrial laboratories, so a stronger competition with thermal recrystallization at temperatures above 100 K might be expected there. A theoretical model of this disruption process has been studied by Mastrapa and Brown [2002]. Given the slight increase in ice temperature and significant decrease in radiation flux as you move away from Jupiter, we can envision a balance between thermal kinetic crystallization and radiolytic disruption, favoring amorphous ice on Europa, and crystalline ice on Callisto, with Ganymede falling in between. The intrinsic magnetic field of Ganymede diverts much of the local plasma flux into the higher latitudes. This fact has been used to support the idea that the polar brightening seen on Ganymede is not a polar cap from molecules transported from the warm equatorial latitudes, but is rather locally derived frost from sputtering by the higher polar radiation levels [Johnson, 1997]. If this is the case, we would expect to see more amorphous ice in these polar regions and more crystalline ice in the equatorial region of Ganymede.

2. Data

[6] The NIMS instrument is an imaging spectrometer that created images by scanning a mirror in one dimension and using slow instrument (scan platform) motion in the other dimension [Carlson et al., 1992]. There are 408 available wavelengths that could be measured, but only 17 were captured at any moment. The spectral resolution (full-width at half-maximum) is ~ 0.026 μm from 1.0–5.3 μm and 0.013 μm from 0.7–1.0 μm , and the spectral sampling is about half of these numbers in the 408 wavelength mode (Nyquist spectral sampling in that mode). The instrument's field-of-view is ~ 0.5 mrad square, giving a spatial resolution and pixel size of, for example, about 5 km at 10,000 km distance. The scanning mirror typically moved over 20 mirror positions, constituting a "mirror swath". The spectra are built up by stepping the spectrometer grating on each successive mirror swath, acquiring all 408 wavelengths in 24 swaths (or 204 wavelengths in 12 swaths, or 102 wavelengths in 6 swaths, while the grating moves in $2\times$ or $4\times$ larger steps, respectively). All three icy satellites have been widely observed, from globally at 50–100 km spatial resolution, down to local observations at <3 km resolution [McCord et al., 1998]. The spacing between the channels changed during the mission due to radiation damage [McCord et al., 1999b], and we take this into account when

plotting model comparisons. Also, the signal from two of the detectors (1.0–1.25 and 2.4–2.7 μm) was lost during the mission.

3. Water Ice Spectral Features

[7] There are several features in the near-infrared reflection spectrum of water ice that can be used to probe lattice order. These include the narrow temperature-sensitive band at 1.65 μm , which is greatly subdued in warm crystalline or cold amorphous ice [Grundy and Schmitt, 1998; Schmitt *et al.*, 1998] as illustrated in Figure 1a. The fundamental absorption near 3.1 μm appears as a reflection peak in frost spectra. It is broad and weak for amorphous and warm ice [Wood and Roux, 1982; Warren, 1984; Hagen *et al.*, 1981], and stronger with a triplet structure for cold crystalline ice [Bergren *et al.*, 1978; Bertie *et al.*, 1969; Hagen *et al.*, 1981], as shown in Figure 1b. In both cases, the amorphous spectrum is very similar in shape to the warm temperature spectrum. For the Galilean satellites, all the ice is at temperatures colder than 150 K, so it is not possible to confuse amorphous ice with warm ice. Subtle band-center shifts and band-width changes are also apparent for all the infrared bands as a function of temperature and crystal order [Grundy and Schmitt, 1998; Hagen *et al.*, 1981].

[8] The spectral properties of the 3.1- μm band in amorphous ice in particular are highly variable and depend strongly on the exact amount of structural disorder as shown by Figures 5–7 of Hagen *et al.* [1981]. The center wavelength in the Wood and Roux [1982] data we are using for amorphous ice at 80 K (tabulated by Roux *et al.* [1979]) would plot at the top of Figure 5 of Hagen *et al.* [1981], near the earlier amorphous measurements of Hardin and Harvey [1973]. It is much shorter in wavelength than the

comprehensive measurements of both fresh deposited and annealed forms of amorphous ice measured by Hagen *et al.* [1981], and also does not match NIMS spectra of amorphous ice well. A shift of the absorption spectrum by +0.025 μm , and the recalculation of the real index through a Kramers-Kronig integration (Figure 1c), provided results that are consistent with the band center and width for annealed amorphous ice given by Hagen *et al.* [1981], and that agree better with measured spectra.

[9] Model albedo spectra of crystalline water snow were calculated using optical constants from several sources: Grundy and Schmitt [1998] (130 K; also 80 and 110 K in other figures) for 1–2.5 μm , Bergren *et al.* [1978] (150 K) for 2.5–3.4 μm , and Toon *et al.* [1994] (162 K) and Clapp *et al.* [1995] (150 K) for 2.7–5.0 μm . The albedo is

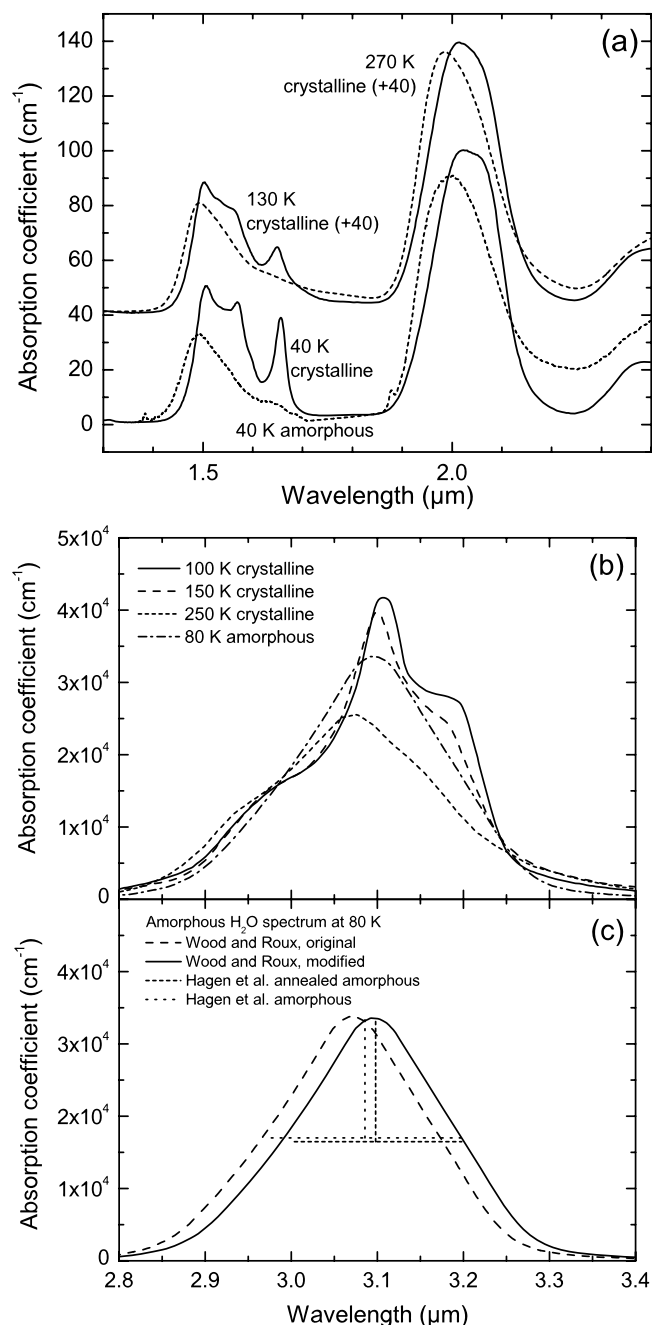


Figure 1. (a) Near-infrared absorption spectra of water ice. The upper curves are offset by +40 cm^{-1} and represent crystalline ice at 130 K (solid line) and 270 K (broken line) as given by Grundy and Schmitt [1998]. The lower curves represent crystalline ice (solid line) [Grundy and Schmitt, 1998] and amorphous water ice (broken line) [Schmitt *et al.*, 1998], both at 40 K. This shows the high variability of the 1.65- μm feature; distinct and strong in crystalline ice and mostly absent in amorphous ice. (b) Absorption spectra of water ice in the region of the fundamental absorption centered near 3.1 μm . The four examples shown are for crystalline ice at 100 K [Bertie *et al.*, 1969], 150 K [Bergren *et al.*, 1978], and 270 K [Warren, 1984] (solid line, dashed line, and short-dash line, respectively), and for amorphous ice at 80 K [Wood and Roux, 1982] (modified) (dot-dash line). (c) Absorption coefficient for amorphous water ice at 80 K. The dashed curve is the original Roux and Wood data, while the solid curve is the modified data with the peak moved 0.025 μm to higher wavelengths. For comparison, the tabular data of Hagen *et al.* [1981], for both annealed and unannealed amorphous ice at 80 K, are represented in graphical form as a vertical line at the band center sitting on a horizontal line extending across the width of the line at 50% of the peak absorption. The dotted lines correspond to unannealed ice, while the short-dashed line corresponds to annealed ice, which is well represented by the modified spectrum.

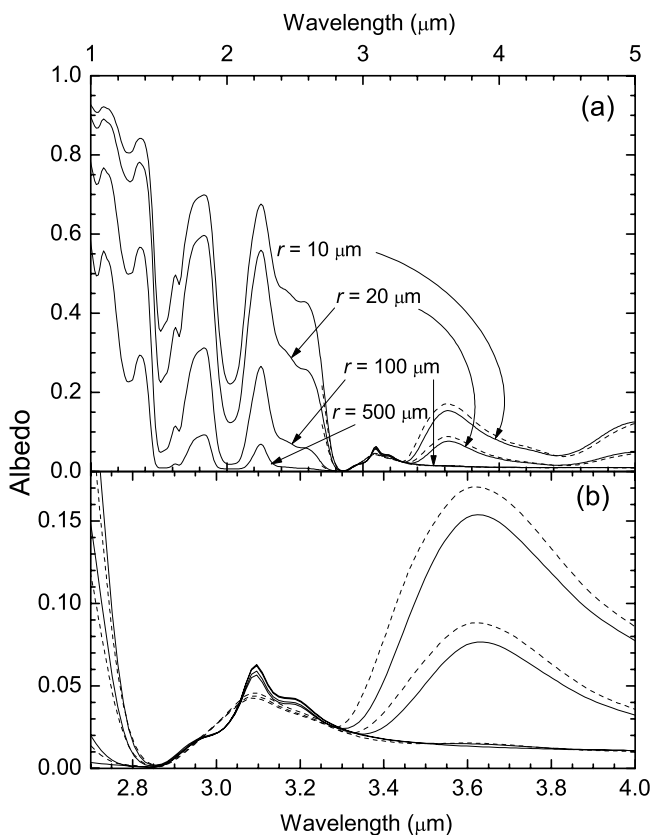


Figure 2. Water snow model spectra sampled at NIMS resolution. (a) The solid lines represent crystalline snow at 130–150 K from 1.0–5.0 μm with grain radii of 10, 20, 100 and 500 μm . The dashed lines represent amorphous snow at 80 K from 2.5–5.0 μm with the same grain radii. The 500- μm spectrum is included to illustrate the saturation of many features between 1.4 and 3 μm for such grain sizes; it is also not different from the 100- μm model beyond 3 μm . (b) The same model spectra in (a), showing detail in the 3- μm region, including the reflection peak from the fundamental absorption. The strength and shape of this feature are not a strong function of grain size, but the three-peaked structure seen in crystalline ice (solid lines) is quite distinct from the broad single peak seen in amorphous ice (dashed lines).

calculated using the delta-Eddington two-stream model described by *Wiscombe and Warren* [1980]. Figure 2a displays model spectra for four different grain radii of crystalline ice, sampled at the resolution of NIMS. Also shown in this figure are models of amorphous snow using the modified 80 K data from *Wood and Roux* [1982] ($\lambda > 2.5 \mu\text{m}$ only). Resampled albedo models like these are used throughout this paper. The non-ice spectra needed for mixture modeling in this work that are available from earlier NIMS publications include the Europa non-ice spectrum from *McCord et al.* [1999a] and the Ganymede non-ice spectrum from *McCord et al.* [2001], and are shown in Figure 3. The NIMS instrument does not have enough spectral resolution to fully represent the 1.65- μm band at temperatures below ~ 130 K, even when all 408 channels are used. The 1.65- μm band arises from ~ 1 mm below the surface. This can be seen in Figure 1a, where the e-folding

optical depth of the band in solid ice at 130 K is on the order of 0.6 mm, so for a more porous layer such as represented by the models presented here, 1 mm is a good estimate of the e-folding optical path to the 1.65- μm band. A consequence of this behavior is that in sufficiently coarse-grained ice (see the 500- μm radius model in Figure 2a), the 1.65- μm band is mostly saturated and not well expressed in the snow spectra. This effect becomes significant for the equatorial Ganymede trailing hemisphere. An expanded view of the 3- μm region is shown in Figure 2b. The 3.1- μm peak comes from the Fresnel reflection off the facets of the water ice grains in the surface, and so is effectively from zero depth. Because of this fact, the strength and shape of the 3.1- μm peak does not vary significantly with grain size, as long as the grains are larger than a few microns in size. For our purposes, amorphous surface ice can be qualitatively identified by a generally broad and featureless 3.1- μm reflection peak, compared to the three-peaked structure in the crystalline spectrum (Figure 2b).

4. Results

[10] The results are grouped by satellite, with determinations that require areal averaging because of high noise during Europa observations or low signal (from ice features)

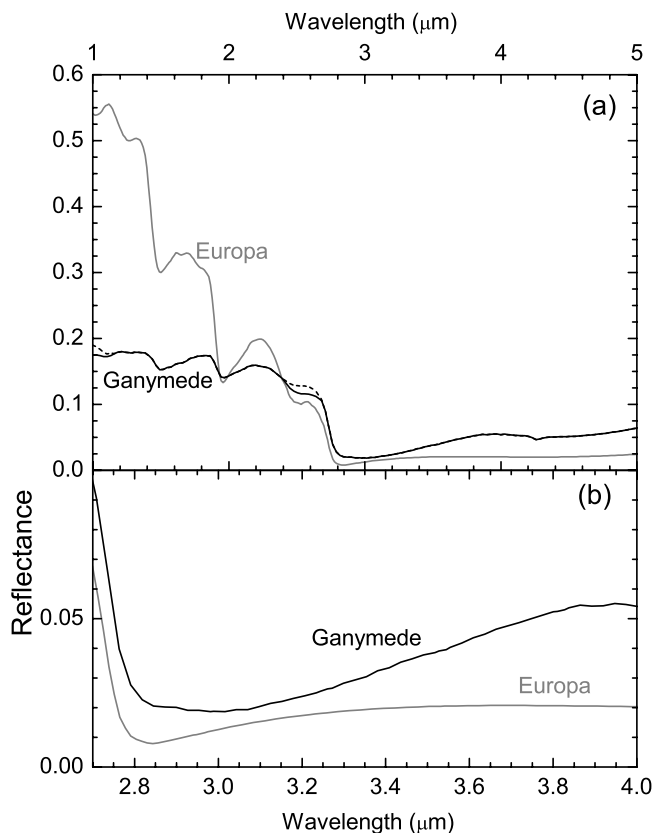


Figure 3. Non-ice spectra for Europa and Ganymede from earlier studies that are used here. The Ganymede spectrum (black line) from *McCord et al.* [1999a] has been modified (broken lines) in the <1.4 and 2.5 – $2.7 \mu\text{m}$ regions as a result of the model fits shown later in this work. The Europa non-ice spectrum (gray line) is from *McCord et al.* [1998]. Non-ice spectra for Callisto are derived here and shown later.

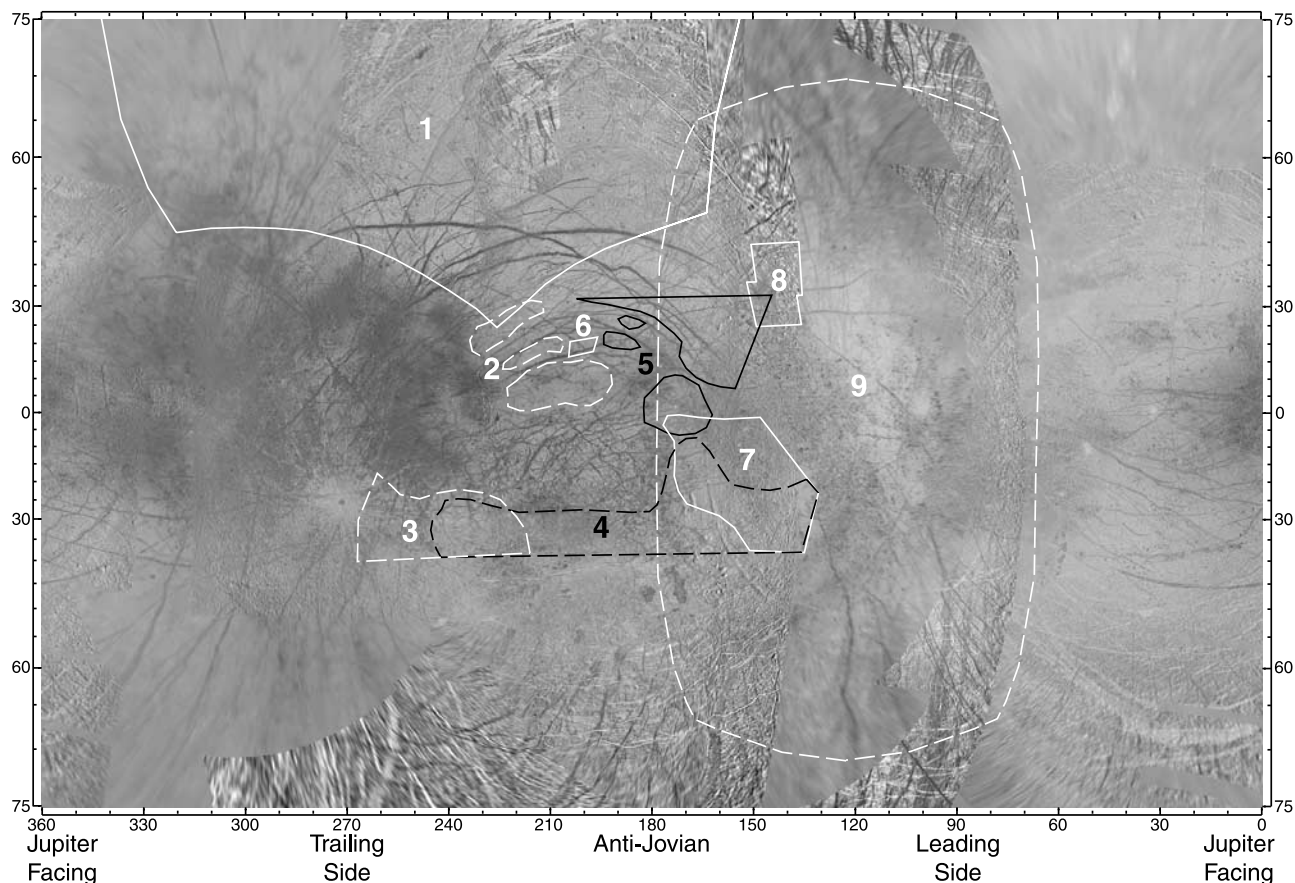


Figure 4. Photomosaic map of Europa with regions outlined where NIMS observations were used to make the average spectra shown in Figure 5. The map is a Mercator projection between $\pm 75^\circ$ latitude and covering $0\text{--}360^\circ$ west longitude, and is made from Galileo images. The areas marked 6 and 8 are the complete NIMS observations from which a subset of icy pixels, impossible to show at this scale, were taken. The other areas represent the approximate actual areas averaged from other lower spatial resolution observations.

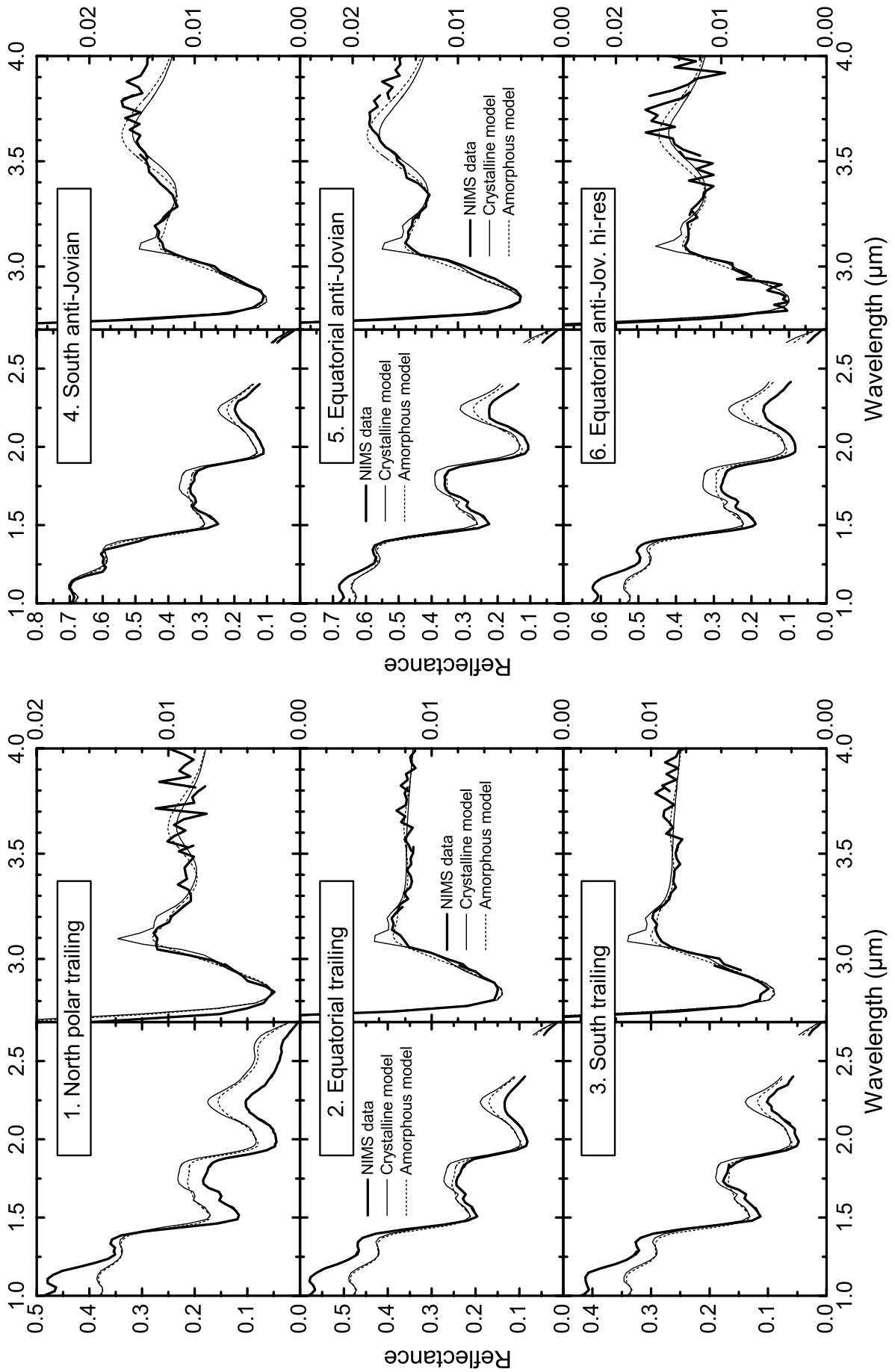
during Callisto observations, treated first. The better quality Ganymede spectra can be analyzed almost pixel-by-pixel, presenting a much more involved analysis. We will present a summary using global scale observations of Ganymede in this paper.

[11] The NIMS observations are analyzed by comparison to model spectra, using the ice spectra detailed above and non-ice spectra from earlier work or determined here (for Callisto). The models are always sampled on the same wavelengths as the observations they are compared to, and all the observations shown here have either 12 or 24 samples per detector throughout. The scaling numbers given in tabular data associated with the figures are supplied for completeness, although the values may be quantitative only in a relative sense (0.3 implies more ice than 0.1, if the non-ice components are similar). However, since the spectra are a combination of albedo (ice) and reflectance at one lighting geometry (non-ice) scaled to reflectance at a different lighting geometry, there is no way to arrive at absolute abundances without more information.

4.1. Europa

[12] Most NIMS observations of Europa are marred by large numbers of spikes caused by radiation on the detec-

tors. These effects can be much reduced if robust averages are taken of many pixels [McCord *et al.*, 1999a]. Since we are primarily looking at the low-reflectance $3.1\text{-}\mu\text{m}$ region, we used this technique here for regions of 100 or more pixels. We find that the low-latitude trailing side shows few strong water ice features [McCord *et al.*, 1999a], so our search is limited to high latitude regions and the equatorial leading side. Nine average spectra have been constructed from five NIMS observations and represent the areas outlined on a photomosaic map (Figure 4). Regions 2 and 5 are disjoint sets of 3 and 4 parts, respectively. Regions 2–5 and 7 are from one particularly low-noise observation in orbit 6. This set of observations provides good coverage of the icy regions on Europa except for longitudes $0\text{--}60^\circ$ W and the trailing side south pole. Calibrated average reflectance (I/F) spectra from the nine regions are shown in Figure 5 as heavy solid lines. Models consisting of linear combinations of water snow albedos and the “albedo” of the Europa non-ice spectrum from McCord *et al.* [1999a] (see Figure 2) are constructed to compare to the NIMS spectra. The uncertainty in these averages is estimated by normalizing the spectral data over ~ 10 wavelengths in local ranges to eliminate lighting geometry and other spatial variations, and calculating the standard deviation of this



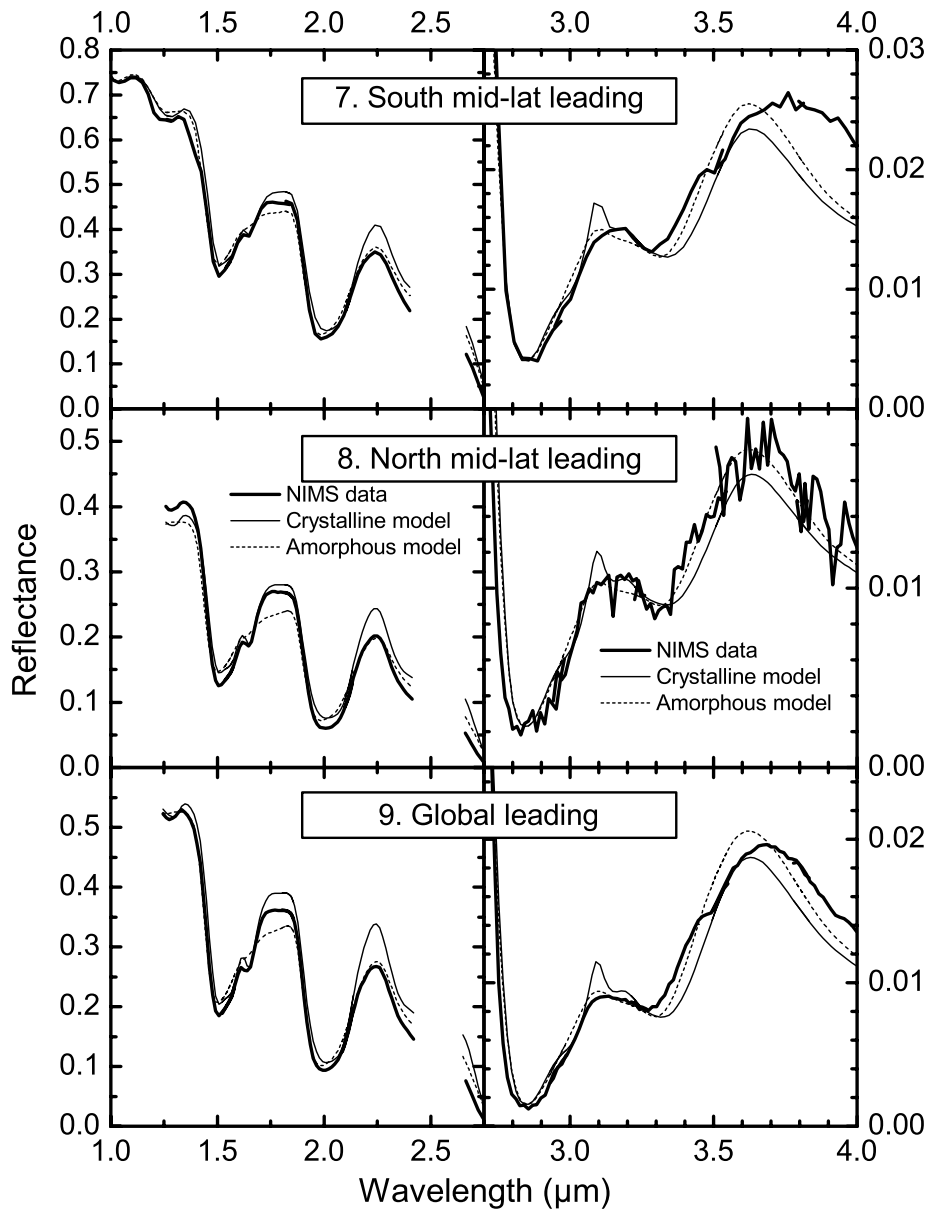


Figure 5. (continued)

normalized ensemble. This uncertainty in reflection for the NIMS average spectra is ≤ 0.005 at $1.65 \mu\text{m}$ and ≤ 0.001 at $3.10 \mu\text{m}$, with regions 2–5 and 7 somewhat below and region 9 well below these maximum uncertainties.

[13] Each spectrum is displayed in two regions, $1.0\text{--}2.75 \mu\text{m}$ (shortwave) and $2.7\text{--}4.0 \mu\text{m}$ (longwave). The shortwave spectra are compared to model spectra using crystalline ice at 80, 110, or 130 K (thin solid line), and at 265 K (thin dashed line) as an analog for amorphous snow

(see Figure 1a). The crystalline models are designed to mimic the band shapes and depths of the NIMS spectra but typically cannot match the overall slopes of the data from various lighting geometries. The amorphous model is made by substituting the amorphous albedo for the crystalline albedo in the same amounts. The longwave models are designed to fit the spectrum as well as possible, and since scattering is not important in this region, the fit is limited mainly by inaccuracies in the optical constants or model

Figure 5. Average Europa ice-rich reflectance spectra and model fits. The average spectra from the nine areas shown in Figure 4 are plotted as heavy, solid lines in each of nine panels with an identifying label (see also Table 1). Each panel consists of a shortwave segment on the left ($1.0\text{--}2.75 \mu\text{m}$) and a longwave segment on the right ($2.7\text{--}4.0 \mu\text{m}$) with different vertical scales. On the shortwave panels, the thin solid line represents a model with the best band shape (see text) using crystalline ice while the thin dashed line represents the same model with amorphous ice. On the longwave panels, the thin dashed line represents a model with the best fit using amorphous ice while the thin solid line is the same model with crystalline ice. The models used are detailed in Table 1.

Table 1. Europa Observations and Models

Description	NIMS Observation Name	Number of Pixels Averaged	Pixel Scale, km	Shortwave Model ^a	Longwave Model ^b
1. North polar trailing	G1NHILAT	467	79	0.15 I (20 μm 80K), 0.45 NI	0.165 I (50 μm), 0.25 NI
2. Equatorial trailing	E6TERINC	427	47	0.15 I (50 μm 110K), 0.65 NI	0.11 I (200 μm), 0.46 NI + 8×10^{-4}
3. South trailing	E6TERINC	556	47	0.16 I (50 μm 110K), 0.38 NI	0.10 I (200 μm), 0.36 NI
4. South anti-Jovian	E6TERINC	880	47	0.24 I (100 μm 110K), 0.92 NI	0.15 I (37 μm), 0.50 NI - 0.001
5. Equatorial anti-Jovian	E6TERINC	782	47	0.35 I (20 μm 130K), 0.60 NI	0.17 I (37 μm), 0.49 NI
6. Equatorial anti-Jovian hi-res	E6SUCOMP2	361	4.7	0.27 I (20 μm 110K), 0.53 NI	0.16 I (40 μm), 0.43 NI
7. South mid-lat. leading	E6TERINC	408	47	0.47 I (16 μm 130K), 0.57 NI	0.18 I (20 μm), 0.46 NI
8. North mid-lat. leading	G7TYREMA	1489	12	0.35 I (20 μm 110K), 0.22 NI	0.12 I (20 μm), 0.39 NI - 0.001
9. Global leading	E11MxxHR	336-1481	200-300	0.48 I (20 μm 110K), 0.32 NI	0.14 I (16 μm), 0.29 NI - 0.001

^aI is ice, with grain radius and temperature as specified; NI is Europa non-ice spectrum (Figure 3).

^bI is ice, with grain radius as specified; NI is Europa non-ice spectrum (Figure 3).

albedo of the components. The observations and the details of the model fits are given in Table 1.

[14] Generally, the models show that the Fresnel surface reflection (3.1 μm) is best represented by amorphous ice, although the majority of the data (areas 2, 3, 4, 7 and 8) indicate a broader peak shape compared to the amorphous model with a flatter top and a center with a longer wavelength. This shape is nothing like the narrow peak of the crystalline model, however, and probably represents an amorphous form with different properties from the laboratory ices. The other four areas match the amorphous model well. On the other hand, the shortwave spectra are usually best modeled with pure crystalline ice mixed with the Europa non-ice spectrum. These spectral features arise from depths ≤ 1 mm, so crystalline features here do not contradict the probable amorphous nature of the grain surface detected at 3.1 μm . The apparent strength of the 1.65- μm feature in pure water snow is weakened by mixing with the non-ice spectrum, but it could also be muted by mixing with amorphous ice. Using amorphous ice mixtures generally leads to a much poorer match to the overall shape of the measured spectrum. However, some of the measured spectra indicate that some amorphous ice at depth may be necessary to improve the fit (e.g., the flat 2.2- μm peak in areas 1-6 and the weaker 1.65- μm feature and greater asymmetry of the 2- μm absorption in areas 7-9). The 1.65- μm feature matches the data very well in areas 1-6, while the amorphous snow model shows no band in these areas. If the amorphous nature of the surface extends to a depth much less than 1 mm (so the crystalline shape of the 1.65- μm band is not affected), the higher-absorbing spectral regions near the 2- μm band might assume a more amorphous shape. The ice model grain sizes vary from 10 μm to >100 μm , with most of the models needing grain radii of 20-50 μm . The grain radii and ice/non-ice amounts do not exactly agree between the shortwave and long wave models, mainly because the scaling of albedo to bidirectional reflectance in these two regions is different (especially the strength of the Fresnel reflection, which varies quite differently from volume scattered reflection over the range of lighting geometries).

4.2. Callisto

[15] The NIMS spectra of Callisto are high quality, but the typical areal exposure of ice on Callisto is only about 10% [Spencer, 1987; Roush *et al.*, 1990; McCord *et al.*,

1998], making the spectral features of the ice, especially the 3.1- μm peak, weak. We have approached this problem by averaging the brightest (iciest) pixels in an observation, and subtracting a scaled non-ice average spectrum, taken from darker (less icy) parts of the observation with the residual amount of water ice removed. This technique serves to isolate the water ice features much better. Uncertainty and error in water ice modeling for the least icy pixels has only minor effects on the resulting non-ice spectrum because of the very small amount of water ice in those spectra. The scaling is necessary because the groups of dark and bright pixels are typically from widely separated parts of an observation with very different lighting geometries. The scaling functions also were not constant across the 2.7- μm drop-off, also due probably to the different reflectance in these contrasting wavelength regions under different lighting geometries. The scaling functions were derived by making a trial bright non-ice spectrum from the difference between the bright spectrum and a plausible scaled ice model. This difference is then divided into the non-ice spectrum from the dark average and smoothed (often using simple line segments) so as to have no specific water ice features and no steep slopes except for the 2.7- μm drop-off. Although there are some inflections in these scaling functions, they are generally smooth and flat near the water ice spectral features investigated here and do not effect the interpretation of these features. The five Callisto observations analyzed here are outlined on a photomosaic map of Callisto in Figure 6. These examples span the leading and trailing hemispheres and the polar regions of Callisto. The number of bright and dark pixels averaged, the surface resolution of the observation, and rough scaling factors are given in Table 2. The complete wavelength-dependent scaling factors for the non-ice spectrum in each of the five observations are displayed in Figure 7. Calibrated average reflectance (I/F) spectra from the bright and dark parts of each of the five regions are shown in Figure 8 as heavy solid and dashed lines, respectively. Also shown are the non-ice spectrum obtained from the dark average, and the scaled non-ice spectrum subtracted from the bright average to get the water ice component of the bright spectrum (heavy dotted line). Against this spectrum are plotted two model fits representing crystalline and amorphous ice (thin solid and thin dashed lines, respectively). The estimated uncertainty of the NIMS average reflection, calculated from normalized spectra (in the same way as for Europa, above),

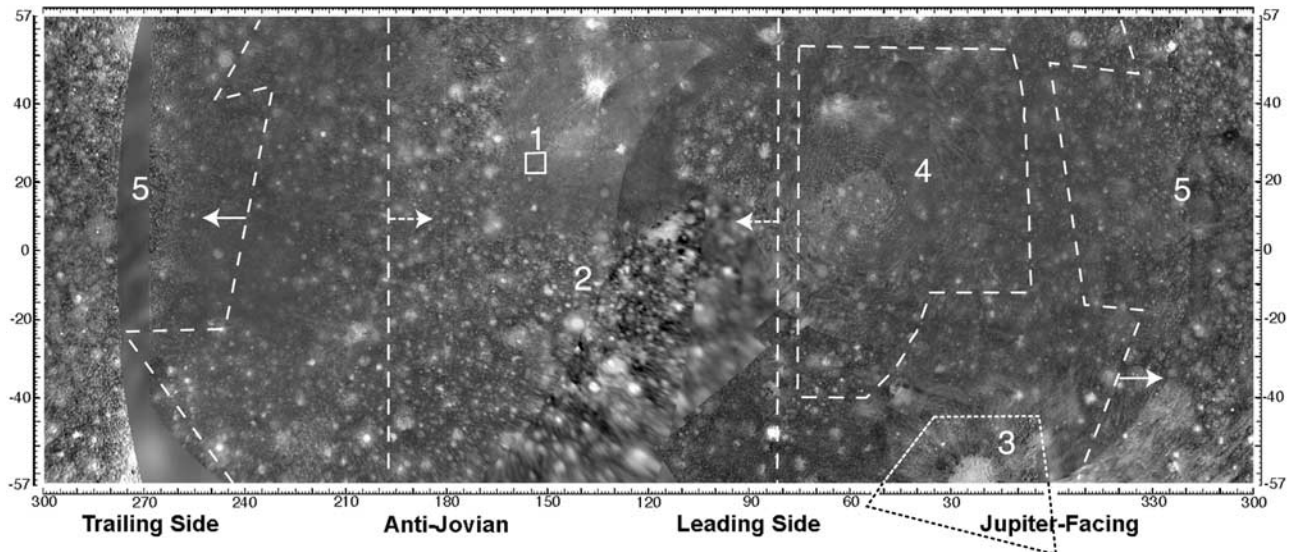


Figure 6. Photomosaic map of Callisto with regions outlined where NIMS observations were used to make the average spectra shown in Figure 8. The map is a Mercator projection between $\pm 57^\circ$ latitude and covering $0\text{--}360^\circ$ west longitude, and is made from Voyager and Galileo images. The numbers correspond to the entries in Table 2 and the parts of Figure 8. Groups of bright (icy) and dark (non-icy) pixels are selected from each area depicted for this analysis.

is approximately ≤ 0.001 near $1.65\ \mu\text{m}$ and ≤ 0.0002 near $3.10\ \mu\text{m}$.

[16] Each spectrum is displayed, as before, in two regions, $1.0\text{--}2.75\ \mu\text{m}$ (shortwave) and $2.7\text{--}4.0\ \mu\text{m}$ (longwave). The shortwave spectra are compared to model albedo spectra using crystalline ice at 110 or 130 K, and at 265 K as an analog for amorphous snow. The longwave spectra do not include the dark pixel average, and the bright average and non-ice spectra are plotted scaled by 2–4 times (as indicated) or on a separate axis scale (for observation 3). The crystalline models are adjusted by selecting grain size(s), temperature, and scaling to fit the band shapes and depths of the NIMS spectra as well as possible. The amorphous model is made by substituting the amorphous albedo for the crystalline albedo using the same grain size and scaling. The longwave models also are designed to fit the spectrum as

well as possible, but the scaling and sometimes grain size are usually different from the short wave models. This difference arises from the different behavior of Fresnel reflection as a function of lighting geometry compared to the shortwave regions dominated by scattering. The subtle water-ice reflection maximum around $3.6\ \mu\text{m}$ is strongly dependent on grain size (for $r \leq 50\ \mu\text{m}$), and its magnitude is very sensitive to the exact shape of non-ice long-wave spectrum subtracted from the icy average. The details of the model fits are given in Table 2.

[17] For all the areas, the narrow 2–3 peaked $3.1\text{-}\mu\text{m}$ reflection feature typical of fully crystalline ice is readily visible (Figure 8). Despite this apparent ubiquitous crystallinity, the $1.65\text{-}\mu\text{m}$ band in observations 4 and 5 is slightly less strong than the crystalline model fits. In both cases the temperature is primarily set to fit the $1.8\text{-}\mu\text{m}$ continuum, the

Table 2. Callisto Observations and Models

Description	NIMS Observation Name	Number of Pixels Averaged		Pixel Scale, km	Approximate Scaling Factor for Dark Non-ice to Bright Non-ice (See Figures 7 and 8)		Shortwave Model ^a	Longwave Model ^b
		Bright (Icy)	Dark (Non-icy)		Shortwave	Longwave		
1. Mid-lat. anti-Jovian hi-res	C3ARINGS	89	143	6.0	1.14	0.94	0.0867 (0.77 $100\ \mu\text{m}$ + 0.23 $1\ \text{mm}$, 110 K)	0.0556 ($50\ \mu\text{m}$)
2. Global leading	C3GLOBAL	161	261	100	1.13	0.69	0.066 (0.76 $20\ \mu\text{m}$ + 0.24 $200\ \mu\text{m}$, 130 K)	0.05 ($100\ \mu\text{m}$)
3. High-lat. Jovian	G8ADLIND	101	139	18	0.99	0.40	0.09 ($22\ \mu\text{m}$, 110 K)	0.055 ($22\ \mu\text{m}$)
4. Global anti-Jovian leading	C9VALHAL	98	114	60.5	1.73	1.25	0.05 ($50\ \mu\text{m}$, 130 K)	0.07 ($50\ \mu\text{m}$)
5. Global trailing (south)	E14GLOBAL	105	100	115	0.75	0.64	0.133 (0.54 $10\ \mu\text{m}$ + 0.46 $100\ \mu\text{m}$, 110 K)	0.09 (0.54 $10\ \mu\text{m}$ + 0.46 $100\ \mu\text{m}$)

^aIce model, a scaled albedo with grain radius and temperature as specified.

^bIce model, a scaled albedo with grain radius as specified.

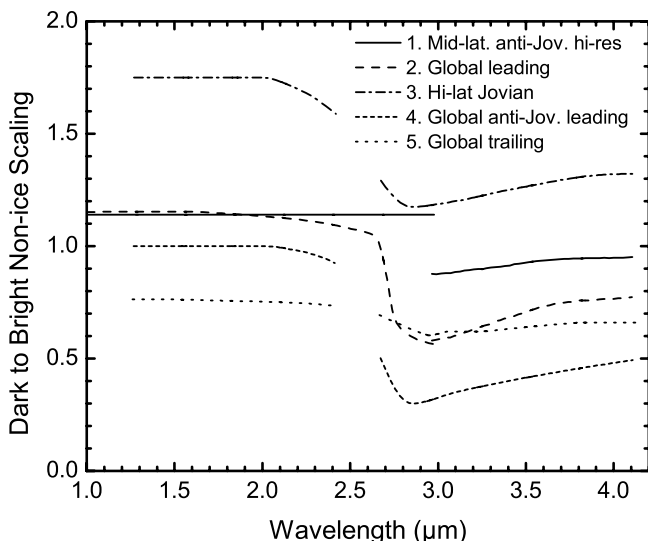


Figure 7. Scaling functions used to scale the dark (low-ice) non-ice spectrum to use as the non-ice component for the bright (icy) spectrum for the five examples shown in Figure 8, as indicated by the legend.

shape of which is correlated to the strength of the 1.65- μm line. In these examples, it appears that the ice at 1 mm depth is >10 K warmer than at the deeper location corresponding to the continuum, or that there is some mixture of amorphous ice at the 1-mm depth. The non-ice spectrum could also be changed (requiring a weak absorption near 1.7 μm) so that the 1.8- μm continuum and 1.65- μm band are consistent with a single warmer temperature. The warmer 1-mm layer implies thermal gradients of $>\pm 10$ K mm^{-1} , too large for a normal thermal profile except for the case of very small effective thermal inertia. This gradient is also too high and the warm layer too shallow to correspond to any reasonable solid-state greenhouse process [Matson and Brown, 1989].

4.3. Ganymede

[18] We have analyzed several global NIMS Ganymede observations [e.g., Hansen *et al.*, 2001], but two global observations that cover three quarters of the surface are all that are needed to demonstrate the properties of the ice on Ganymede (see Table 3). These observations have been analyzed in the 3.1- μm region on a pixel by pixel basis to determine the distribution of crystalline and amorphous ice.

[19] To map the variation of ice over the surface, a (usually) cubic continuum is fitted between ~ 2.85 and ~ 3.35 μm , and subtracted from the data. The resulting shape is normalized to lie between 0 and 1 and compared to one of two pairs of functions (Figure 9) defined at zero

and one crystallinity factor (CF). One pair of functions is derived by subtracting a cubic continuum from the model crystalline and amorphous spectra (Figure 9a), and the other pair was determined from end-members found in the anti-Jovian global observation (Figure 9b). The end-members were determined primarily by looking at the shape of the spectrum in the 3.1–3.25- μm region (smooth for amorphous, and low at 3.1 μm and high at 3.2 μm for crystalline).

[20] Each normalized, continuum-subtracted spectrum in the observation is compared to a linear sum [$\text{CF} \times \text{xtal} + (1 - \text{CF}) \times \text{amor}$] of the crystalline and amorphous shapes which provides the best fit in a least squares sense. The pair of functions that provides the best fit is adopted. The CF is allowed to range above 1 and below 0 to achieve better fits than if it were constrained. The spectral shapes resulting from out-of-range CF do not become significantly distorted or unrealistic until $\text{CF} < -1$ or $\text{CF} > 2$, so CF is usually allowed to vary from -0.7 to 1.7 (see examples in Figure 10, where $\text{CF} < 0$ and $\text{CF} > 1$). Fits that have especially large residuals (the sum of data minus model squared) were improved by averaging 3×3 and 5×5 pixels in the projected images. Most of the pixels in the final maps have average uncertainties (the square root of the residual divided by the number of points) of better than 1.5×10^{-4} in units of reflectance. Figure 10 shows examples of good (residuals of $\sim 0.7 \times 10^{-4}$) crystalline (a) and amorphous (b) fits from the data.

[21] The global CF distribution is shown in Figure 11, with (a) showing the anti-Jovian hemisphere (G1GLOBAL) and (b) showing the trailing hemisphere (E6GLOBAL). Each observation includes a Galileo/Voyager based context image on the left and a color map of crystallinity on the right (dark blue = amorphous, light blue-green = 50-50 mixture, dark red = crystalline). Note the finely detailed structure in the crystalline-amorphous distribution, a characteristic which extends down to a scale of at least a few 10s of km, on the basis of the analysis of higher spatial resolution observations. The genesis of these patterns is not a simple relationship to factors such as albedo, for example, and is not very clear at this time. A detailed discussion of these patterns is outside the scope of this paper.

[22] A statistical analysis of this data is shown in Figure 12, which demonstrates some easy to see and meaningful global-scale patterns in the data. Histograms of the distribution of crystalline and amorphous ice are shown for the complete observation (anti-Jovian (a) and trailing (b) hemispheres) and for six latitude sectors in each hemisphere ($>45^\circ\text{S}$, 45°S to 15°S , 15°S to 0° , 0° to 15°N , 15°N to 45°N , and $>45^\circ\text{N}$). The anti-Jovian hemisphere shows an overall balance between crystalline and amorphous ice (CF a little less than 0.5) and a clear enhancement of crystalline ices at low latitudes and amorphous ices at

Figure 8. Average Callisto ice-rich and ice-poor reflectance spectra, non-ice spectral estimates, and ice-rich ice component with model fits. The average spectra from the five observations shown in Figure 6 are plotted as thick, solid (ice-rich) or dashed (ice-poor) lines in each of five panels with an identifying label (see also Table 2). Non-ice spectral estimates are shown as thin, dashed (ice-poor) and dotted (ice-rich, scaled from the ice-poor non-ice spectrum) lines. The ice component of the ice-rich spectrum is shown as a heavy, dotted line, and compared to crystalline (thin, solid lines) and amorphous (thin, dashed lines) ice models. The models are detailed in Table 2. Each panel consists of a shortwave segment on the left (1.0–2.75 μm) and a longwave segment on the right (2.7–4.0 μm) with different vertical scales.

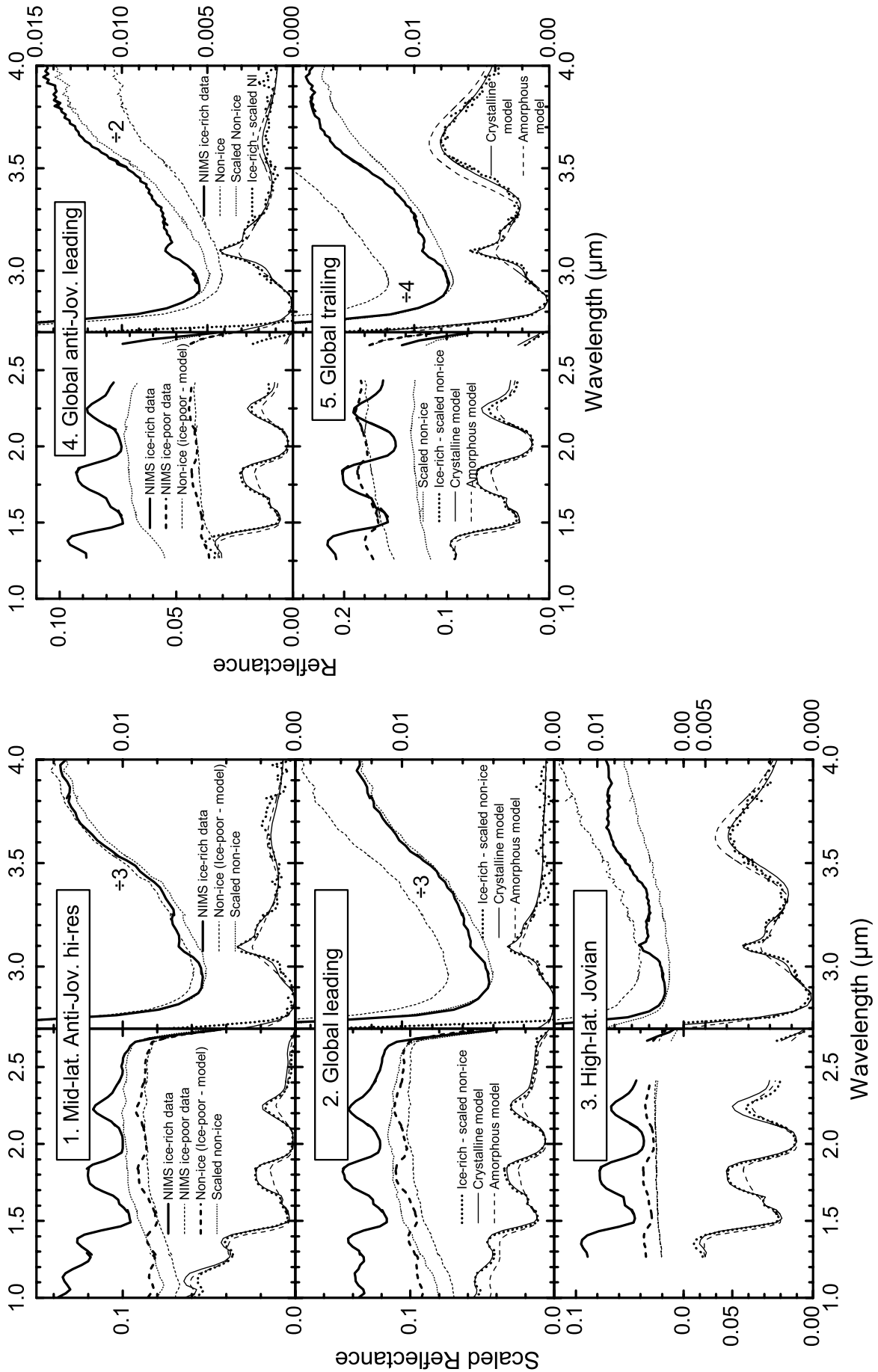


Table 3. Ganymede Observations and Models

Description	NIMS Observation Name	Number of Pixels Averaged	Pixel Scale, km	Non-ice Models and Scaling ^a		Shortwave Ice Model ^b	Longwave Ice Model ^b
				Shortwave	Longwave		
1. Anti-Jovian equatorial crystalline	G1GLOBAL	4	115	1.14 ^c	0.87 ^c	0.145 (100 μm , 110 K)	0.13 (100 μm)
2. Anti-Jovian equatorial amorphous	G1GLOBAL	6	115	1.00 ^c	0.75 ^c	0.25 (0.5 50 μm + 0.5 500 μm , 110 K)	0.25 (0.5 50 μm + 0.5 500 μm)
3. Anti-Jovian polar crystalline	G1GLOBAL	10	115	0.27	0.24	0.33 (14 μm , 110 K)	0.21 (18 μm)
4. Anti-Jovian polar amorphous	G1GLOBAL	9	115	0.2	0.13	0.43 (0.8 10 μm + 0.2 100 μm , 110 K)	0.25 (0.6 10 μm + 0.4 100 μm)
5. Trailing equatorial crystalline	E6GLOBAL	10	160	1.04 ^c	1.10 ^c	0.13 (350 μm , 110 K)	0.13 (350 μm)
6. Trailing equatorial amorphous	E6GLOBAL	7	160	0.97 ^c	0.98 ^c	0.115 (420 μm , 110 K)	0.13 (420 μm)
7. Trailing polar crystalline	E6GLOBAL	4	160	0.3 G + 0.06 E ^d		0.17 (0.7 10 μm + 0.3 100 μm , 110 K)	0.11 (38 μm)
8. Trailing polar amorphous	E6GLOBAL	6	160	0.19 G + 0.14 E ^d	0.23 G + 0.16 E ^d	0.26 (0.6 10 μm + 0.4 50 μm , 110 K)	0.125 (0.3 10 μm + 0.7 100 μm)

^aUsing the Ganymede non-ice spectrum in Figure 3, except where indicated.

^bScaled albedo with grain radius (and temperature for shortwave) as specified.

^cApproximate; see Figure 15.

^dWhere G and E refer to the Ganymede and Europa non-ice spectra (Figure 3), respectively.

high latitudes (CF \sim 0.5 near the equator and CF $<$ 0.4 at the poles). The trailing hemisphere is predominantly amorphous (CF \sim 0.35) and the lowest median CF is near the equator (CF \sim 0.15 at 0–15°N), while the highest is near the pole (CF \sim 0.6 at $<$ 45°S), in sharp contrast to the distribution on the anti-Jovian hemisphere. The cause of these global patterns is likely the radiation environment, dominated by corotational flow on the trailing side, and modulation of magnetospheric bombardment by the intrinsic magnetic field of Ganymede (preferentially directing ions and electrons into the polar regions) on the anti-Jovian hemisphere.

[23] To display a clean 3.1- μm peak in Ganymede spectra, several pixels needed to be averaged. Eight average spectra from groups of 4–10 pixels (see Table 3) were selected out of the global observations to illustrate both crystalline and amorphous surface ice in both equatorial and polar latitudes for each observation. The eight areas are

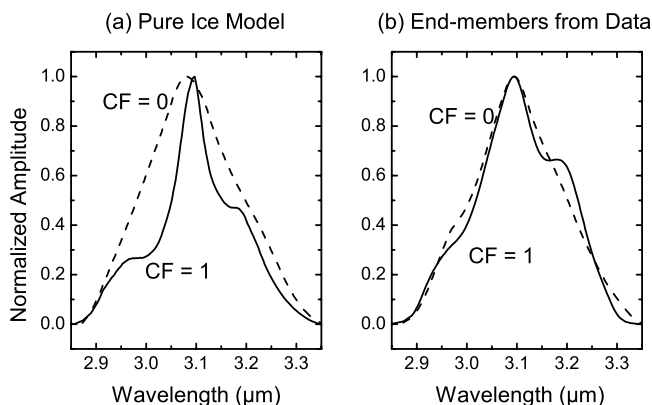


Figure 9. Shape models used in crystalline-amorphous mapping on Ganymede. Shapes for crystalline (CF = 1) and amorphous (CF = 0) ice from theoretical albedo models are shown in (a), while shapes from end-member searching of the G1GLOBAL data set (using primarily the shape differences between 3.1 and 3.25 μm) are shown in (b).

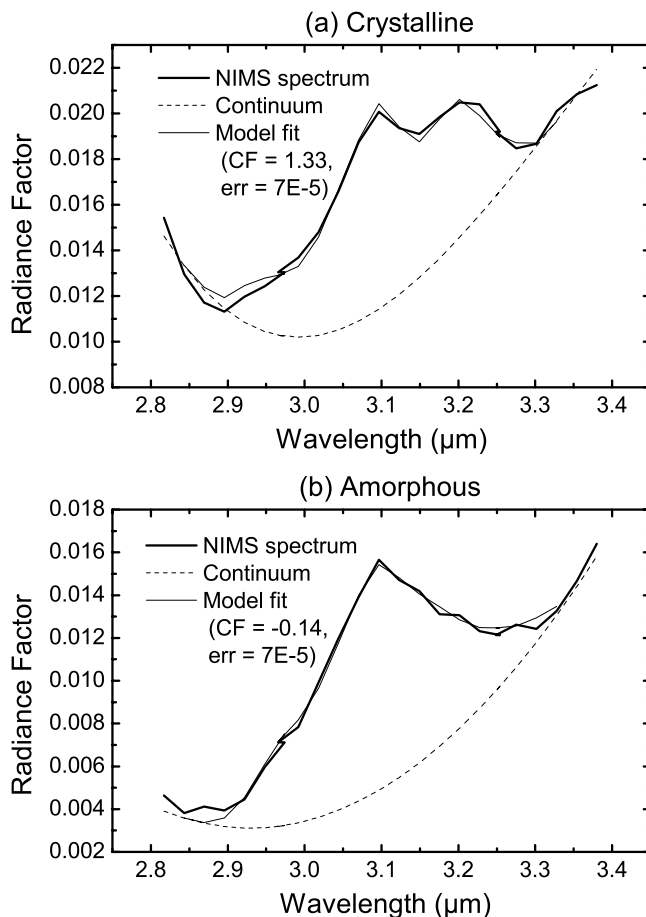


Figure 10. Example of spectral fits of the Ganymede spectra (heavy lines) to crystalline (a) and amorphous (b) models (thin lines) plus a cubic continuum (dashed lines). The crystallinity factor (CF) and least squares residual (err) for the model fits are indicated.

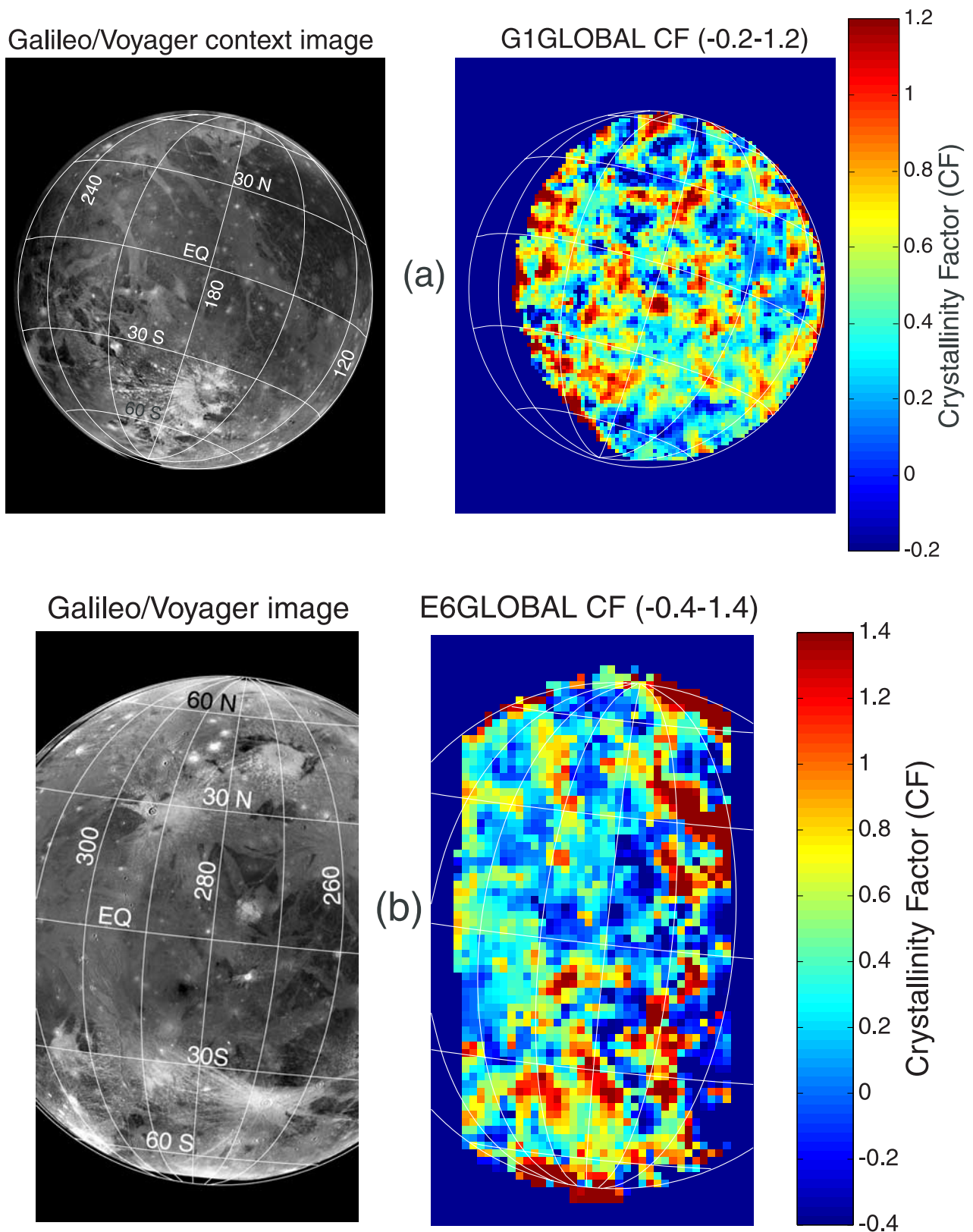


Figure 11. Context images and crystalline/amorphous maps for (a) the anti-Jovian hemisphere (G1GLOBAL), and (b) the trailing hemisphere (E6GLOBAL). The images are projected from Galileo and Voyager mosaics. The color bars on the right show the range of crystallinity factor (CF) in the map.

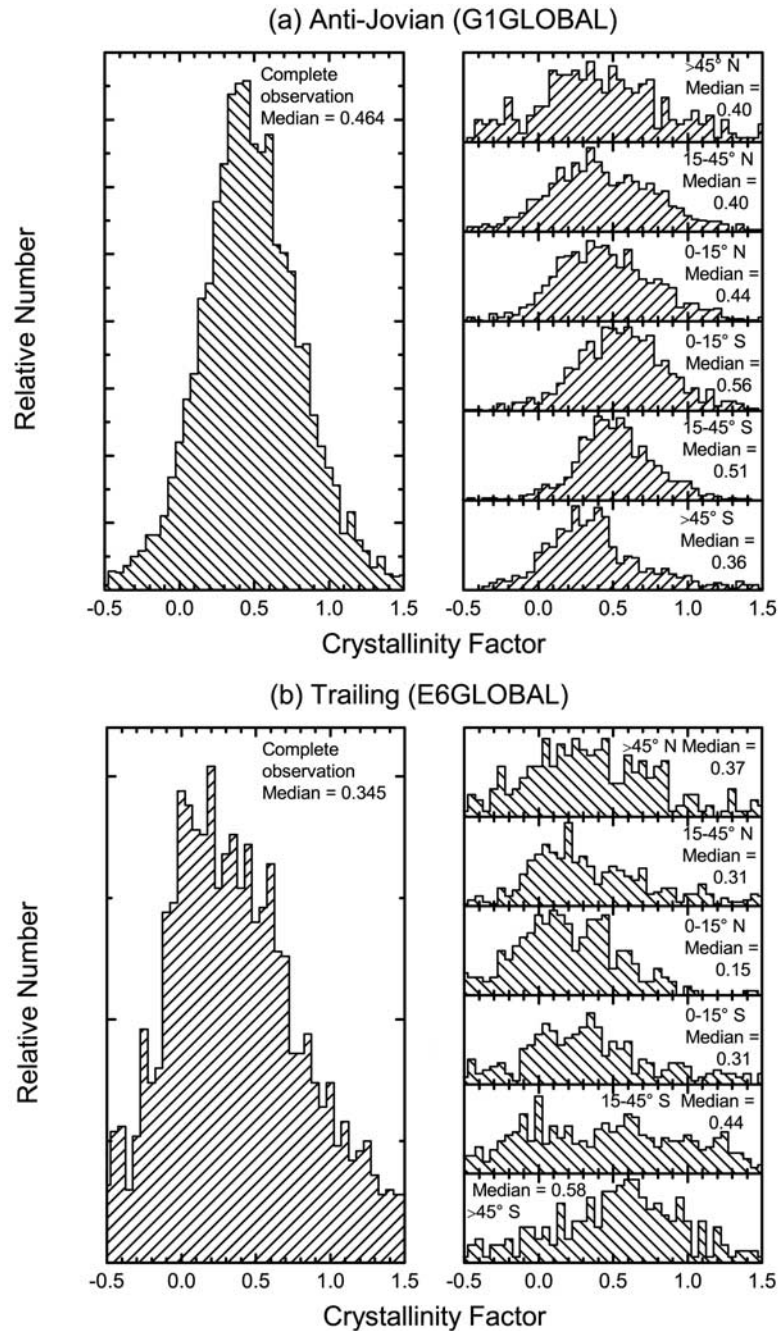


Figure 12. Histograms of the distribution of crystallinity factor for (a) the anti-Jovian hemisphere (G1GLOBAL), and (b) the trailing hemisphere (E6GLOBAL). A histogram of the whole observation is on the left, while six stacked histograms representing the distribution in six zonal regions is on the right for each observation. The median of the distribution is given for each data group along with the latitude range covered in each plot on the right.

located on a photomosaic map of Ganymede in Figure 13, with numbers that correspond to the entries in Table 3 and the panels of Figure 14. The calibrated average reflectance (I/F) spectra are shown as thick, solid lines in each panel of Figure 14. A non-ice spectrum is matched to each average by scaling the spectra in Figure 3 as given in Table 3, so that the water ice component can be derived by subtraction (linear mixing is assumed). The scaling for the eight polar spectra was wavelength independent in two segments on either side

of $2.7 \mu\text{m}$. Wavelength dependent scaling (Figure 15) is necessary for equatorial spectra because the spectra are mostly from regions with different lighting geometries from the place where the non-ice spectrum was derived (on the trailing side). The scaling was derived similarly to the case for Callisto, using a trial observation non-ice ratio to the standard non-ice component. The anti-Jovian observation was all at a different geometry, so all its spectra need a scaling much different from one. As for Callisto, the scaling

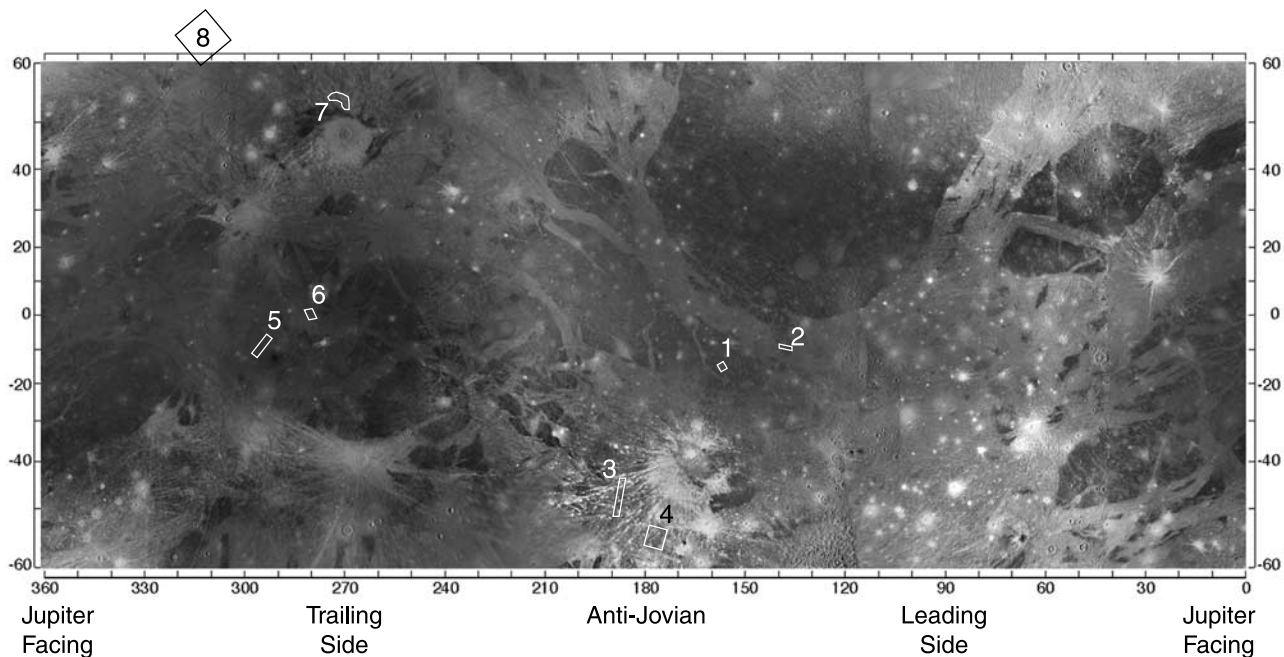


Figure 13. Photomosaic map of Ganymede with regions outlined where NIMS observations were used to make the average spectra shown in Figure 14. The map is a Mercator projection between $\pm 60^\circ$ latitude and covering $0\text{--}360^\circ$ west longitude, and is made from Voyager and Galileo images. Each area comprises 4–10 pixels from two global scale observations, with the numbers corresponding to those given in Table 3 and Figure 14. The odd numbers correspond to regions of crystalline surface ice and the even numbers to regions of amorphous ice.

functions were not constant across the $2.7\text{-}\mu\text{m}$ drop-off, and display broad overall shapes, but they do not effect the interpretation of the narrow water ice bands for the same reasons given in the Callisto analysis. The scaled non-ice spectrum is shown in each panel as a thin, dotted line. The water ice component of the average spectrum (average minus scaled non-ice) is shown as a thick, dotted line. Against this spectrum are plotted two model fits representing crystalline and amorphous ice (thin solid and thin dashed lines, respectively). The estimated uncertainty of the NIMS average reflection, calculated from normalized spectra (in the same way as for Europa and Callisto, above), is approximately ≤ 0.002 at $1.65\ \mu\text{m}$ and ≤ 0.0004 at $3.10\ \mu\text{m}$.

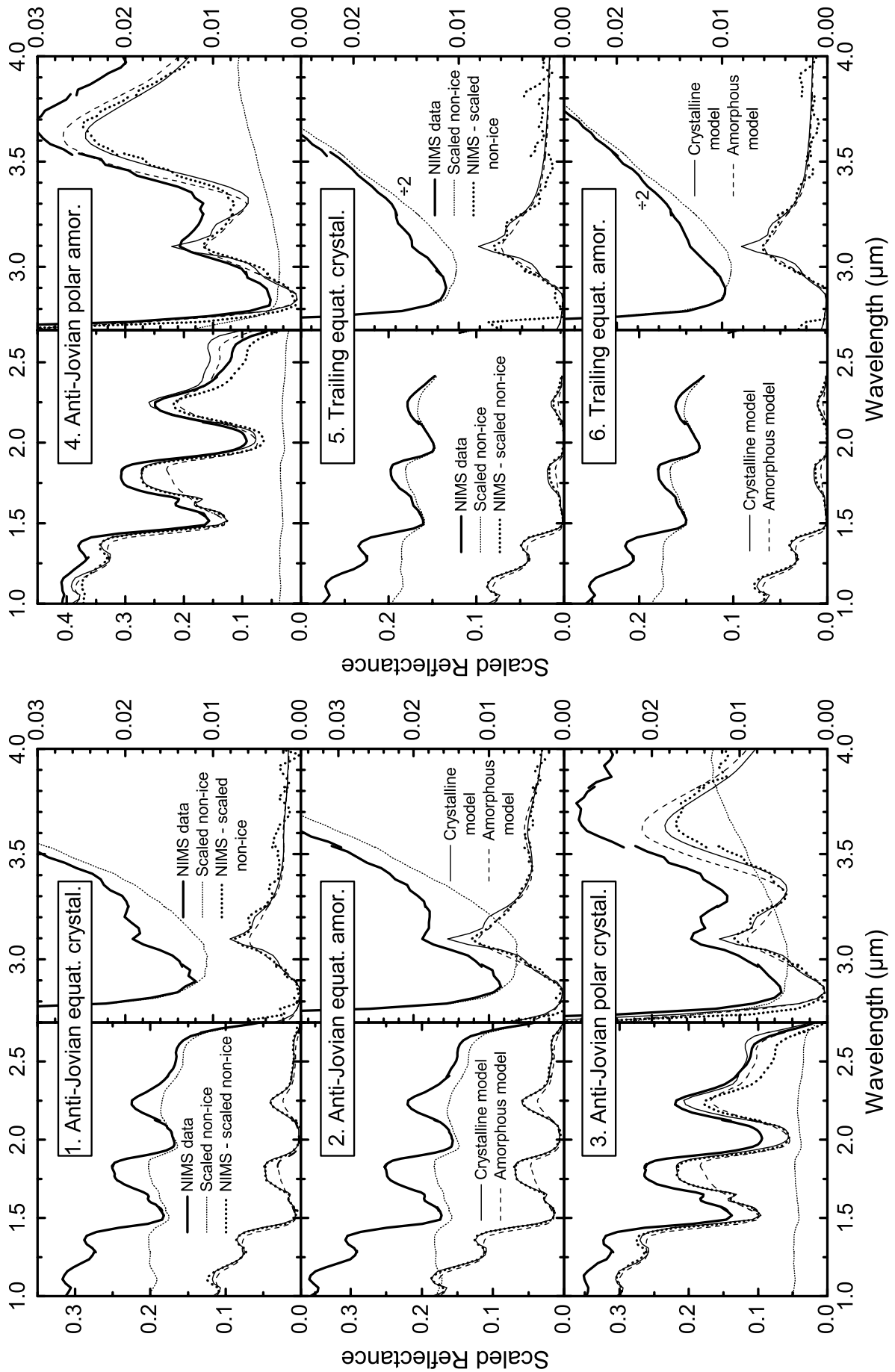
[24] Each spectrum is displayed, as before, in two regions, $1.0\text{--}2.75\ \mu\text{m}$ (shortwave) and $2.7\text{--}4.0\ \mu\text{m}$ (long-wave). The shortwave spectra are compared to model albedo spectra using crystalline ice at 110 K, and at 265 K as an analog for amorphous snow. The crystalline models are adjusted by selecting grain size(s), temperature, and scaling to fit the band shapes and depths of the NIMS ice-component spectra as well as possible. The amorphous model is made by substituting amorphous albedo for the crystalline albedo using the same grain size and scaling. The longwave models also are designed to fit the spectrum as well as possible, but the scaling and sometimes grain size are different from the short wave models in the same way as for Callisto. The larger amounts of ice on Ganymede make finding and fitting the water-ice reflection maximum around $3.6\ \mu\text{m}$ much easier than for Callisto. All the details for the model fits are given in Table 3.

[25] For the crystalline areas, the narrow 2–3 peaked $3.1\text{-}\mu\text{m}$ reflection feature typical of fully crystalline ice is

readily visible (Figure 14). The peak height in two cases (3 and 5) is slightly below the model prediction, but the $3.2\text{-}\mu\text{m}$ shoulder is strong in all four cases. In the amorphous areas, the $3.1\text{-}\mu\text{m}$ reflection feature is quite similar to the models, although sometimes (2 and 4) there is a little bump at $2.95\ \mu\text{m}$ similar to the crystalline feature. The vast majority of the spectra show mixed features, so it is not surprising that few spectra have a purely amorphous or crystalline character. The $1.65\text{-}\mu\text{m}$ band and $1.8\text{-}\mu\text{m}$ continuum are well fit by the 110 K crystalline ice model in almost all cases. For the trailing equatorial regions (5 and 6), the ice is too large-grained to exhibit much of a $1.65\text{-}\mu\text{m}$ band, but the crystalline nature is guaranteed by the properties of the continuum (a slightly higher temperature ice may be appropriate for the continuum in these trailing equatorial spectra). The trailing side polar (7 and 8) $1.65\text{-}\mu\text{m}$ bands are slightly weaker than the model. As for Callisto, the temperature is primarily set to fit the $1.8\text{-}\mu\text{m}$ continuum, correlated to the strength of the $1.65\text{-}\mu\text{m}$ line, implying that a shallow layer of ice is warmer than the models, or that there is some mixture of amorphous ice at that depth. Again, very high implied temperature gradients favor the partially amorphous explanation.

5. Discussion and Conclusions

[26] These observations show that there is a balance between radiolytic disruption and thermal ordering of the surface ice on the Galilean satellites. The surface ice, as indicated by the $3.1\text{-}\mu\text{m}$ first surface Fresnel reflection, implies crystalline ice on Callisto, apparently amorphous ice on Europa, and a mixture of ices on Ganymede. This pattern is broadly consistent with the expected distribution



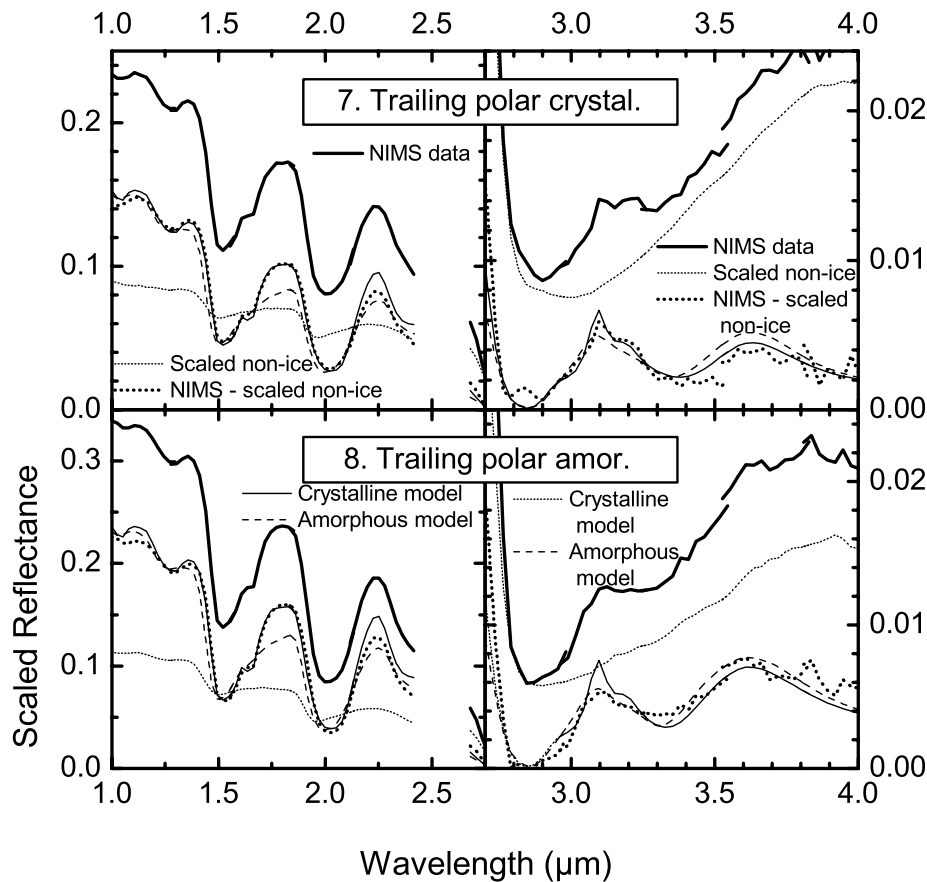


Figure 14. (continued)

and intensity of radiation in the Jovian system [Cooper *et al.*, 2001]. This radiation density is roughly 10 times higher at Ganymede than at Callisto, and 32 times higher at Europa than at Ganymede. The closed field lines of the intrinsic magnetic field of Ganymede protect the lower latitudes from much of the local Jovian electron flux, but heavy and very energetic ions and neutralized corotation ions can penetrate to these lower latitudes. Modeling implies that a population of keV magnetospheric protons also penetrates the closed field lines on the trailing apex [Cooper *et al.*, 2001]. The broad, global patterns of crystalline and amorphous surface ice on Ganymede are consistent with the expected distribution of energetic magnetospheric ions and neutrals, but the detailed distribution implies additional control by geologic or other factors. It seems likely that the crystallization timescale is almost identical to the radiolytic disruption timescale on Ganymede, so that very small factors can greatly influence the equilibrium.

[27] The maximum (equatorial mid-day) temperature of the ice on the three satellites varies by no more than 20 K

[Grundy *et al.*, 1999], but the timescale for crystallization is an exponential function of temperature and varies by a factor of $\sim 10^5$ [Jenniskens *et al.*, 1998] between 105 K and 125 K. The ice temperature varies by 10 K or more from the equator to the pole on any one satellite, which implies a significant variation in crystallization rate across a single satellite. This strong function suggests that the crystallization and amorphization balance at a well defined point in radiation flux/temperature space. This explains the dichotomy between the ice on Europa and Callisto, but is contrary to the mixed ice distribution seen on Ganymede, where mixed ices occur in two distinct regions of higher temperature and lower flux at the equator, and lower temperature and higher flux at the poles. Perhaps other factors are acting here that match the temperature variation of the disruption and crystallization functions near their crossover, such as a temperature variation in disruption efficiency that is independent from thermal crystallization rates.

[28] All three icy satellites show predominantly crystalline ice at millimeter depths demonstrated by the behavior

Figure 14. Average Ganymede reflectance spectra, non-ice spectral estimates, and ice component with model fits. The average spectra from the eight regions observed (see Figure 13) are plotted as thick, solid lines in each of the eight panels with an identifying label (see Table 3). Non-ice spectral estimates, scaled (see Table 3 and Figure 15) from the Ganymede and Europa non-ice end-members (Figure 3) are shown as thin, dotted lines. The ice component of the spectrum (observation average minus scaled non-ice) is shown as a heavy, dotted line, and compared to crystalline (thin, solid lines) and amorphous (thin, dashed lines) ice models. The models are detailed in Table 3. Each panel consists of a shortwave segment on the left (1.0–2.75 μm) and a longwave segment on the right (2.7–4.0 μm) with different vertical scales.

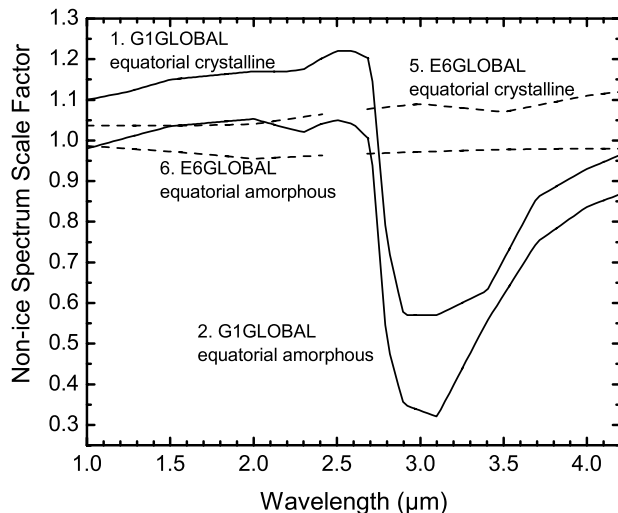


Figure 15. Scaling functions for the Ganymede non-ice spectrum shown in Figure 3 used in the four equatorial region Ganymede average spectra (numbers 1, 2, 5, and 6) shown in Figure 14, as indicated. The non-ice spectrum is taken from a trailing side midlatitude region, and scales simply to other trailing side spectra, while higher contrast scaling is needed to match observations with different lighting conditions in the other hemisphere. The four polar spectra need only constant scaling for <2.7 and >2.7 μm , as indicated in Table 3.

of their 1.65- μm bands and 1.8- μm continua. The reflection from depths represented by continua on either side of the 2- μm band and the 1.65- μm band implies some mixture with amorphous ice for Europa spectra, and either some amorphous ice or significantly warmer ice for some Ganymede and Callisto spectra. The maximum temperature gradient from the “solid state greenhouse” of Matson and Brown [1989] is 1–2 K mm^{-1} , much less than is needed to explain the weak 1.65- μm line in some of the Ganymede and Callisto spectra ($>\pm 10 \text{ K mm}^{-1}$). The spectral resolution of NIMS (26 nm) is mostly able to represent the 1.65- μm band (23–30 nm) well, but the variation with temperature is much more subtle than with fully resolved spectra.

[29] The spatial scale of the Callisto and Europa ice mapping is too large to know whether any small areas of crystalline ice on Europa or small areas of amorphous ice on Callisto may exist. This remains for future spectral measurements that have an improved signal-to-noise and spatial scale compared to NIMS. If such areas are found, it might imply a significant non-equilibrium condition (e.g., recently emplaced ice), on the basis of the conclusions of this work.

[30] **Acknowledgments.** This work was supported by grant NAG5-8983 from the National Aeronautics and Space Administration Office of Space Science through the Jupiter Science Data Analysis Program. The manuscript was improved through reviews by Bob Carlson and an anonymous reviewer, as well as from an early review by Karl Hibbitts.

References

Baratta, G. A., A. C. Castorina, G. Leto, M. E. Palumbo, F. Spinella, and G. Strazzulla (1994), Ion irradiation experiments relevant to the physics of comets, *Planet. Space Sci.*, *42*, 759–766.

- Bergren, M. S., D. Schuh, M. G. Sceats, and S. A. Rice (1978), The OH stretching region infrared spectra of low density amorphous solid water and polycrystalline ice Ih, *J. Chem. Phys.*, *69*, 3477–3482.
- Bertie, J. E., and E. Whalley (1964), Infrared spectra of ices Ih and Ic in the range 4000 to 350 cm^{-1} , *J. Chem. Phys.*, *40*, 1637–1645.
- Bertie, J. E., and E. Whalley (1967), Optical spectra of orientationally disordered crystals. II. Infrared spectrum of ice Ih and ice Ic from 360 to 50 cm^{-1} , *J. Chem. Phys.*, *46*, 1271–1284.
- Bertie, J. E., H. J. Labbe, and E. Whalley (1969), Absorptivity of ice I in the range 4000–30 cm^{-1} , *J. Chem. Phys.*, *50*, 4501–4520.
- Calvin, W. M., and R. N. Clark (1991), Modeling the reflectance spectrum of Callisto 0.25 to 4.1 μm , *Icarus*, *89*, 305–317.
- Carlson, R. W., P. R. Weissman, W. D. Smythe, J. C. Mahoney, and the NIMS Science and Engineering Team (1992), Near-infrared mapping spectrometer experiment on Galileo, *Space Sci. Rev.*, *60*, 457–502.
- Carlson, R. W., et al. (1996), Near-infrared spectroscopy and spectral mapping of Jupiter and the Galilean satellites: Results from Galileo’s initial orbit, *Science*, *274*, 385–388.
- Clapp, M. L., R. E. Miller, and D. R. Worsnop (1995), Frequency dependent optical constants of water ice obtained directly from aerosol extinction spectra, *J. Phys. Chem.*, *99*, 6317–6326.
- Clark, R. N. (1982), Implications of using broadband photometry for compositional remote sensing of icy objects, *Icarus*, *49*, 244–257.
- Clark, R. N., and T. B. McCord (1980), The Galilean satellites: New near-infrared spectral reflectance measurements (0.65–2.5 μm) and a 0.325–5 μm summary, *Icarus*, *41*, 323–339.
- Clark, R. N., R. B. Singer, P. D. Owensby, and F. P. Fanale (1980), Galilean satellites: High precision near-infrared spectrophotometry (0.65–2.5 μm) of the leading and trailing sides, *Bull. Am. Astron. Soc.*, *12*, 713–714.
- Clark, R. N., F. P. Fanale, and M. J. Gaffey (1986), Surface composition of satellites, in *Satellites*, edited by J. Burns and M. S. Matthews, pp. 437–491, Univ. of Ariz. Press, Tucson.
- Cooper, J. F., R. E. Johnson, B. H. Mauk, H. B. Garrett, and N. Gehrels (2001), Energetic ion and electron irradiation of the icy Galilean satellites, *Icarus*, *149*, 133–159.
- Grundy, W. M., and B. Schmitt (1998), The temperature-dependent near-infrared absorption spectrum of hexagonal H_2O ice, *J. Geophys. Res.*, *103*, 25,809–25,822.
- Grundy, W. M., M. W. Buie, J. A. Stansberry, and J. R. Spencer (1999), Near-infrared spectra of icy outer solar system surfaces: Remote determination of H_2O ice temperatures, *Icarus*, *142*, 536–549.
- Hagen, W., A. G. G. M. Tielens, and J. M. Greenberg (1981), The infrared spectra of amorphous solid water and ice Ic between 10 and 140 K, *Chem. Phys.*, *56*, 367–379.
- Handa, Y. P., D. D. Klug, and E. Whalley (1988), Energies of phases of ice at low temperature and pressure relative to ice Ih, *Can. J. Chem.*, *66*, 919–924.
- Hansen, G. B., and T. B. McCord (2000), Amorphous and crystalline ice on the Galilean satellites: A balance between thermal and radiolytic processes (abstract), *Lunar Planet. Sci.* [CD-ROM], XXXI, abstract 1630.
- Hansen, G. B., R. T. Pappalardo, and T. B. McCord (2001), The distribution of crystalline and amorphous ice on Ganymede (abstract), *Geophys. Res. Abstr.*, *3*, 7465.
- Hardin, A. H., and K. B. Harvey (1973), Temperature dependence of the ice I hydrogen bond spectral shifts—I. The vitreous to cubic ice I phase transformation, *Spectrochim. Acta*, *29A*, 1139–1151.
- Jenniskens, P., D. F. Blake, and A. Kouchi (1998), Amorphous water ice, in *Solar System Ices*, edited by B. Schmitt, C. de Bergh, and M. Festou, pp. 199–240, Kluwer Acad., Norwell, Mass.
- Johnson, R. E. (1997), Polar “caps” on Ganymede and Io revisited, *Icarus*, *128*, 469–471.
- Johnson, T. V., and T. B. McCord (1971), Spectral geometric albedo of the Galilean Satellites, 0.3 to 2.5 μm , *Astrophys. J.*, *169*, 589–594.
- Kouchi, A., T. Yamamoto, T. Kozasa, T. Kuroda, and J. M. Greenberg (1994), Conditions for condensation and preservation of amorphous ice and crystallinity of astrophysical ices, *Astron. Astrophys.*, *290*, 1009–1018.
- Kuiper, G. P. (1961), Limits of completeness, in *Planets and Satellites*, edited by G. P. Kuiper and B. M. Middlehurst, pp. 575–591, Univ. of Chicago Press, Chicago, Ill.
- Mastrapa, R. M. E., and R. H. Brown (2002), Modeling amorphization of crystalline water ice on Europa, Ganymede, and Callisto (abstract), *Bull. Am. Astron. Soc.*, *34*, 881.
- Matson, D. L., and R. H. Brown (1989), Solid-state greenhouses and their implications for icy satellites, *Icarus*, *77*, 67–81.
- McCord, T. B., et al. (1998), Non-water-ice constituents in the surface material of the icy Galilean satellites from the Galileo near infrared mapping spectrometer investigation, *J. Geophys. Res.*, *103*, 8603–8626.
- McCord, T. B., et al. (1999a), Hydrated salt minerals on Europa’s Surface from the Galileo near-infrared mapping spectrometer investigation, *J. Geophys. Res.*, *104*, 11,827–11,852.

- McCord, T. B., G. B. Hansen, J. H. Shirley, and R. W. Carlson (1999b), Discussion of the 1.04- μm water ice absorption band in the Europa NIMS spectra, *J. Geophys. Res.*, *104*, 27,157–27,162.
- McCord, T. B., G. B. Hansen, and C. A. Hibbitts (2001), Hydrated salt materials on Ganymede's surface: Evidence of an ocean below, *Science*, *292*, 1523–1525.
- Moore, J. M., et al. (1999), Mass movement and landform degradation on the icy Galilean satellites: Results of the Galileo nominal mission, *Icarus*, *140*, 294–312.
- Moroz, V. I. (1965), Infrared spectrophotometry of the Moon and the Galilean satellites of Jupiter (in Russian), *Astron. Z.*, *42*, 1287–1295. (*Trans. Sov. Astron. A. J.*, Engl. Transl., *9*, 999–1006, 1965.)
- Orton, G. S., J. R. Spencer, L. D. Travis, T. Z. Martin, and L. K. Tamppari (1996), Galileo photopolarimeter-radiometer observations of Jupiter and the Galilean satellites, *Science*, *274*, 389–391.
- Pilcher, C. B., S. T. Ridgway, and T. B. McCord (1972), Galilean satellites: Identification of water frost, *Science*, *178*, 1087–1089.
- Pollack, J. B., F. C. Witteborn, E. F. Erickson, D. W. Strecker, B. J. Baldwin, and T. E. Bunch (1978), Near-infrared spectra of the Galilean satellites: Observations and compositional implications, *Icarus*, *36*, 271–303.
- Roush, T. L., J. B. Pollack, F. C. Witteborn, J. D. Bregman, and J. P. Simpson (1990), Ice and minerals on Callisto: A reassessment of the reflectance spectra, *Icarus*, *86*, 355–382.
- Roux, J. A., B. E. Wood, and A. M. Smith (1979), IR optical properties of thin H_2O , NH_3 , and CO_2 cryofilms, *Tech. Rep. AEDC-TR-79-57*, 108 pp., Arnold Eng. Dev. Cent., Arnold Air Force Stn., Tenn.
- Schmitt, B., E. Quirico, F. Trotta, and W. M. Grundy (1998), Optical properties of ices from UV to infrared, in *Solar System Ices*, edited by B. Schmitt, C. de Bergh, and M. Festou, pp. 199–240, Kluwer Acad., Norwell, Mass.
- Sill, G. T., and R. N. Clark (1982), Composition of the surfaces of the Galilean satellites, in *Satellites of Jupiter*, edited by D. Morrison, pp. 174–212, Univ. of Ariz. Press, Tucson.
- Spencer, J. R. (1987), Thermal segregation of water ice on the Galilean satellites, *Icarus*, *69*, 297–313.
- Spencer, J. R., L. K. Tamppari, T. Z. Martin, and L. D. Travis (1999), Temperatures on Europa from Galileo PPR: Nighttime thermal anomalies, *Science*, *284*, 1514–1516.
- Strazzulla, G., G. A. Baratta, G. Leto, and G. Foti (1992), Ion-beam-induced amorphization of crystalline water ice, *Europhys. Lett.*, *18*, 517–522.
- Toon, O. B., M. A. Tolbert, B. G. Koehler, A. M. Middlebrook, and J. Jordan (1994), Infrared optical constants of H_2O ice, amorphous nitric acid solutions, and nitric acid hydrates, *J. Geophys. Res.*, *99*, 25,631–25,654.
- Warren, S. G. (1984), Optical constants of ice from the ultraviolet to the microwave, *Appl. Opt.*, *23*, 1206–1225.
- Wiscombe, W. J., and S. G. Warren (1980), A model for the spectral albedo of snow, I. Pure snow, *J. Atmos. Sci.*, *37*, 2712–2733.
- Wood, B. E., and J. A. Roux (1982), Infrared optical properties of thin H_2O , NH_3 , and CO_2 cryofilms, *J. Opt. Soc. Am.*, *72*, 720–728.

G. B. Hansen, Pacific Northwest Division, Planetary Science Institute, Department of Earth and Space Science, University of Washington, Johnson Annex A, Box 351310, Seattle, WA 98195-1310, USA. (ghansen@rad.ess.washington.edu)

T. B. McCord, Pacific Northwest Division, Planetary Science Institute, 22 Fiddler's Road, Winthrop, WA 98862, USA.